Science Advances

AAAS

advances.sciencemag.org/cgi/content/full/1/9/e1500396/DC1

Supplementary Materials for

Catenary optics for achromatic generation of perfect optical angular momentum

Mingbo Pu, Xiong Li, Xiaoliang Ma, Yanqin Wang, Zeyu Zhao, Changtao Wang, Chenggang Hu, Ping Gao, Cheng Huang, Haoran Ren, Xiangping Li, Fei Qin, Jing Yang, Min Gu, Minghui Hong, Xiangang Luo

Published 2 October 2015, *Sci. Adv.* **1**, e1500396 (2015)
DOI: 10.1126/sciadv.1500396

This PDF file includes:

S1. Design of the optical catenaries. The catenary apertures are composed of space-variant slits derived from the spin-orbit interaction in inhomogeneous anisotropic media *(12)*. Here we define ξ as the angle between the slit and the coordinate axis, and Φ as the geometric phase. For LCP illumination ($\sigma = 1$), the relation between Φ and ξ can be written as $\Phi = 2\xi$ (see equation (S7) for detail). In general, the design procedure of the catenary apertures consists of two steps. First, write explicitly the space-variant angle $\xi(x, y)$ according to the required phase distributions by using the geometric relation $\xi(x, y) = \Phi(x, y)/2$; Then, integrate the tangent of the angle, i.e. $\tan\xi(x, y)$, over Cartesian or polar coordinates (Fig. S1A). For a linear phase distribution along the x-direction, $dy/dx = \tan(\pi x/\Lambda)$ can be directly integrated over the x-axis to obtain equation (1).

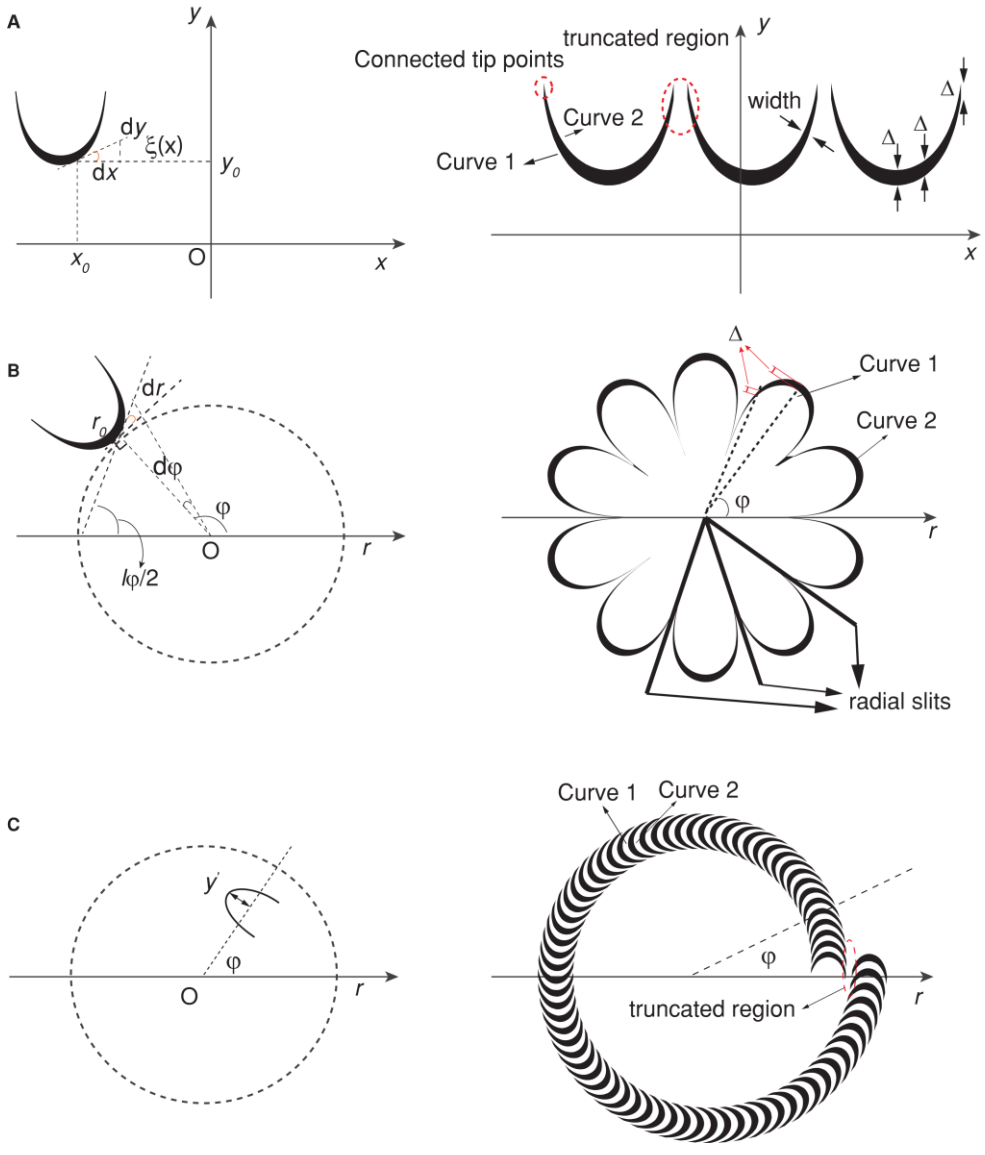

Fig. S1. Schematic of the integration procedures to design the catenaries. (**A**) Linear array in the Cartesian coordinates. Note that the vertical shift of the catenary curve is always Δ, while the width of the catenary aperture varies from place to place. (**B**) Rotated arrays in the polar coordinates for the generation of the OAM beam. (**C**) Rotated arrays in the polar coordinates for the generation of the HOBB and the focused OAM beam. Here curves 1 and 2 denote two adjacent catenary curves with a relative shift along the coordinate axis.

A single catenary aperture can be obtained by shifting equation (1) with Δ along the *y*-direction. Because the value of equation (1) is infinite for $x = \pm\Lambda/2 + m\Lambda$ (m is an integer), the curves are truncated at the two ends with $\Delta x = \Lambda/20$ in practical designs, i.e. the span of x is $(-9\Lambda/20+m\Lambda, 9\Lambda/20+m\Lambda)$. After the truncation, the four tips of the two catenary curves are connected to obtain the catenary aperture (Fig. S1A).

For the generation of OAM, the surface structure should be designed so that the phase distribution is $\Phi(r, \varphi) = l\varphi$. As illustrated in the geometric relation in Fig. S1B, the tangent angle of the curve at a given position (r, φ) with respect to the azimuthal direction is $\xi = l\varphi/2 - \varphi + \pi/2$. Consequently, the equation describing the surface profile can be written as

$$\frac{dr}{rd\varphi} = -\tan\xi = -\tan[\frac{(l-2)\varphi+\pi}{2}]. \tag{S1}$$

By some non-trivial mathematical manipulation, the unique curve for generating OAM could be obtained,

$$\begin{aligned} r &= (r_0 + m\Delta)\exp\left\{\frac{2}{2-l}\ln\left(\left|\sec[\frac{(l-2)\varphi+\pi}{2}]\right|\right)\right\} \\ &= (r_0 + m\Delta)\left(\left|\sec[\frac{(l-2)\varphi+\pi}{2}]\right|\right)^{\frac{2}{2-l}}, m = 0,1,2,3..., \end{aligned} \tag{S2}$$

where $r_0 + m\Delta$ denotes the vertex of a single curve, m is the index of these curves, and Δ is the distance between the adjacent vertexes. In general, the angle "π" in equations (S1) and (S2) can be omitted as shown in equation (2), since it denotes only an azimuthal rotation of the structure. Obviously, equation (S2) has a singularity at $l = 2$ (LCP incidence). In such a specific case, the direct integration of equation (S1) leads to a set of concentric rings.

To obtain a HOBB, the phase distribution is defined as $\Phi(r, \varphi) = k_r r + l_1\varphi$. The corresponding catenary can be constructed by local approximation assuming that the radial and azimuthal components are decoupled. Along each radial direction with constant φ, the governing equation becomes

$$y' = \frac{2}{k_r}\ln\left(\left|\sec\left(\frac{k_r r + l_1\varphi}{2}\right)\right|\right), \tag{S3}$$

where *y'* is illustrated in Fig. S1C.

In the generation of the focused OAM beam, the radial phase distribution is not linear anymore and no analytic curve can be derived. Instead, numerical integration should be applied to obtain the radial curve at a given azimuthal location

$$y' = \int \tan\left(\frac{k\sqrt{r^2 + f^2} + l_2\varphi}{2}\right)dx, \tag{S4}$$

where k is the free-space wave number, f the focal length, and l_2 the topological charge. It should be noted that the curves determined by the equations (S2-S4) need to be truncated to avoid infinite values. At the same time, the tip points of the curves are connected to obtain the final apertures.

Owing to the truncation of the catenaries, there will be blank areas (or truncated regions as shown in Fig. S1) where no light can transmit. If the truncation region has horizontal dimension of $\Lambda/10$, there is a phase jump of about $2\pi/10$. In practical designs, slits can be added between the catenaries to increase the phase continuity along the azimuthal direction. For the samples shown in the left column of Fig. 2, radial slits with a width of 200 nm were inserted between these catenaries. In the samples shown in Fig. 4, A to C, there are spiral and concentric slits with a width of 100 nm.

S2. Geometric phase in subwavelength metallic grating. The physical mechanism of the extraordinary geometric phase in catenary arrays is the anisotropic transmission in the local subwavelength gratings. By using the Jones matrix formalism, the transmission property for polarized light can be easily accessed. First, the Jones matrix for a subwavelength thin metallic grating with period of p, width of $w = p/2$, and main axes along the local u-v coordinates takes the form of

$$J_g = \begin{bmatrix} t_u & 0 \\ 0 & t_v \end{bmatrix}, \tag{S5}$$

where t_u and t_v are the transmission coefficients along the two main axes. Supposing that the u-direction has a rotation angle of ξ with respect to the x-axis, we can obtain the general Jones matrix in the x-y coordinates,

$$\begin{aligned} J_\xi &= \begin{bmatrix} \cos\xi & -\sin\xi \\ \sin\xi & \cos\xi \end{bmatrix} J_g \begin{bmatrix} \cos\xi & \sin\xi \\ -\sin\xi & \cos\xi \end{bmatrix} \\ &= \begin{bmatrix} t_u\cos^2\xi + t_v\sin^2\xi & (t_u - t_v)\sin\xi\cos\xi \\ (t_u - t_v)\sin\xi\cos\xi & t_u\sin^2\xi + t_v\cos^2\xi \end{bmatrix}. \end{aligned} \tag{S6}$$

Finally, the output fields for circular polarized input can be written in a different form:

$$\begin{bmatrix} E_x \\ E_y \end{bmatrix} = \frac{J_\xi}{\sqrt{2}} \begin{bmatrix} 1 \\ i\sigma \end{bmatrix} = \frac{1}{2\sqrt{2}} \left(\left(t_u + t_v\right) \begin{bmatrix} 1 \\ i\sigma \end{bmatrix} + \left(t_u - t_v\right) e^{2i\sigma\xi} \begin{bmatrix} 1 \\ -i\sigma \end{bmatrix} \right), \tag{S7}$$

where $\sigma = \pm 1$ denotes the LCP and RCP, respectively. Therefore, the output fields are composed of two circular polarizations with opposite handedness. The additional phase of the counter-rotating polarization $2\sigma\xi$ is purely geometrical and independent of the working frequency. The conversion efficiency can be then defined as:

$$\eta = \frac{\left|t_u - t_v\right|^2}{\left|t_u - t_v\right|^2 + \left|t_u + t_v\right|^2}, \tag{S8}$$

where $0.5|t_u + t_v|$ and $0.5|t_u - t_v|$ are just the amplitudes of the co-polarized and cross-polarization transmission coefficients for circular polarizations. As indicated by equation (S8), the difference in transmission along the u- and v-directions is essential to obtain high conversion efficiency. If the

anisotropic material is comprised of space-variant half-wave plate, there is $t_u+t_v = 0$ and the efficiency can be as large as 100% *(12)*.

In the following, full-wave calculations are carried out to obtain the t_u and t_v for the catenary aperture. Similar to Fig. 5, the catenary is treated as gratings with varying width w and period p. We calculated the transmission coefficients for different period p, while the width is set as $w = p/2$. The co-polarized and cross-polarized transmission coefficients for CPL are calculated by $0.5|t_u + t_v|$ and $0.5|t_u - t_v|$. As shown in Fig. S2, the transmission coefficients vary with the period at higher frequencies, thus the catenary would also exert amplitude modulation on the incident light. It should be noted that these amplitude fluctuations are much weaker at the low-frequency regime, where the structures are in deep-subwavelength scale and the metals behave more like PECs.

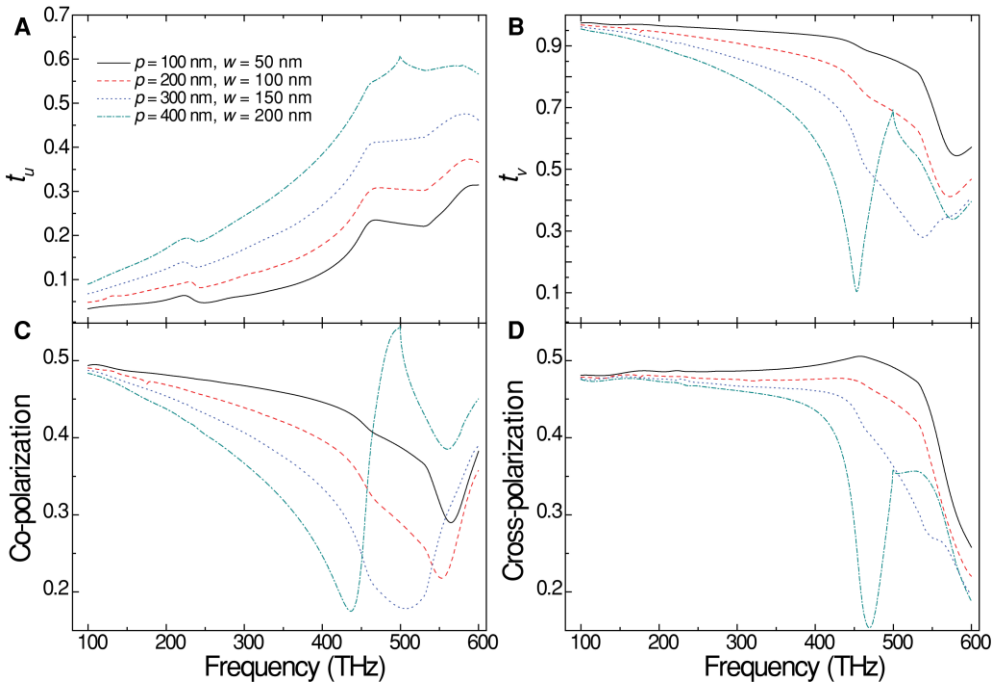

Fig. S2. Transmission coefficients of the subwavelength grating. (A) Transmission coefficients of the light polarized along the *u*-direction. The definitions of the *u*- and *v*-directions are the same as that in Fig. 5. (B) Transmission coefficients of the light polarized along the *v*-direction. (C) Co-polarized transmission for CPL. (D) Cross-polarized transmission for CPL. The periods are varying from 100 nm to 400 nm. The abrupt change for $p = 400$ nm at $f = 500$ THz ($\lambda = 600$ nm) is owing to the diffraction in the substrate, where the dielectric constant is near 1.5 and the effective wavelength in the substrate equals to the period.

S3. Influence of the amplitude modulation. As can be seen in Fig. S2, the amplitude distributions of both the cross-polarized and co-polarized light can be modulated by the catenaries in the high frequency regime. In order to elucidate the amplitude modulation properties, we fabricated another sample which can generate OAM with $l = \pm 1$ (Fig. S3, A and B). As shown in Fig. S3C, the measured intensity patterns agree well the simulations at $\lambda = 632.8$ nm (LCP, $l = -1$). Furthermore, using a quarter-wave plate and a polarizer, we filtered out the co-polarized and cross-polarized fields, as shown in Fig. S3D. Clearly, the co-polarized intensity pattern is not uniform, indicating that diffraction occurs owing to the periodic amplitude modulation. In contrast, the doughnut-shaped

pattern of the cross-polarized component becomes much smoother compared to the case in Fig. S3C, implying that the influence of amplitude modulation of cross-polarized light is rather weak.

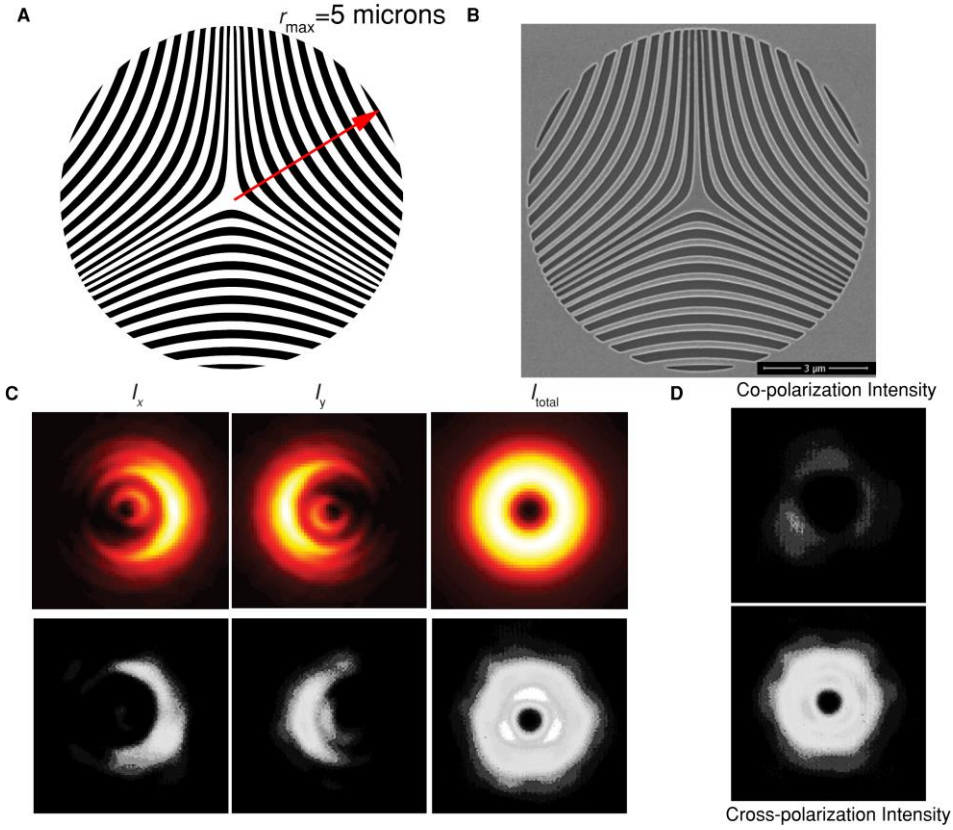

Fig. S3. Design, fabrication, and characterization of the sample with *l* = ±1. (A) Design of the sample. (B) SEM image of the fabricated sample. (C) Comparison of the theoretical and experimental results of the I_x, I_y, and I_{total} at z = 10 μm and λ =632.8 nm for LCP illumination (l = -1). The interferences of the co-polarized and cross-polarized CPL lead to the crescent-like patterns for I_x and I_y. (D) The intensity distributions for the co-polarized (above) and cross-polarized (below) components.